Quantitative appraisal for noise reduction in digital holographic phase imaging

Silvio Montresor[1] and Pascal Picart[1,2,*]

[1]*Université du Maine, CNRS UMR 6613, LAUM, Avenue Olivier Messiaen, 72085 Le Mans Cedex 9, France*
[2]*École Nationale Supérieure d'Ingénieurs du Mans, Rue Aristote, 72085 Le Mans Cedex 9, France*
[*]*pascal.picart@univ-lemans.fr*

Abstract: This paper discusses on a quantitative comparison of the performances of different advanced algorithms for phase data de-noising. In order to quantify the performances, several criteria are proposed: the gain in the signal-to-noise ratio, the Q index, the standard deviation of the phase error, and the signal to distortion ratio. The proposed methodology to investigate de-noising algorithms is based on the use of a realistic simulation of noise-corrupted phase data. A database including 25 fringe patterns divided into 5 patterns and 5 different signal-to-noise ratios was generated to evaluate the selected de-noising algorithms. A total of 34 algorithms divided into different families were evaluated. Quantitative appraisal leads to ranking within the considered criteria. A fairly good correlation between the signal-to-noise ratio gain and the quality index has been observed. There exists an anti-correlation between the phase error and the quality index which indicates that the phase errors are mainly structural distortions in the fringe pattern. Experimental results are thoroughly discussed in the paper.

References and links

1. T. C. Poon, *Digital Holography and Three-Dimensional Display: Principles and Applications* (Springer-Verlag, New York, 2010).
2. P. Picart, *New Techniques in Digital Holography* (ISTE-Wiley, London, 2015).
3. J.W. Goodman, *Speckle Phenomena in Optics* (Roberts and Company Publishers, Greenwood Village, 2006).
4. J. Poittevin, P. Picart, C. Faure, F. Gautier, and C. Pézerat, "Multi-point vibrometer based on high-speed digital in-line holography," Appl. Opt. **54**(11), 3185–3196 (2015).
5. J. Poittevin, P. Picart, F. Gautier, and C. Pézerat, "Quality assessment of combined quantization-shot-noise-induced decorrelation noise in high-speed digital holographic metrology," Opt. Express **23**(24), 30917–30932 (2015).
6. H. A. Aebischer and S. Waldner, "A simple and effective method for filtering speckle-interferometric phase fringe patterns," Opt. Commun. **162**(4-6), 205–210 (1999).
7. Q. Kemao, S. H. Soon, and A. Asundi, "Smoothing filters in phase-shifting interferometry," Opt. Laser Technol. **35**(8), 649–654 (2003).
8. D. C. Ghiglia and M. D. Pritt, *Two-Dimensional Phase Unwrapping: Theory, Algorithms and Software* (Wiley, New York, 1998)
9. Q. Kemao, S. H. Soon, and A. Asundi, "A simple phase unwrapping approach based on filtering by windowed Fourier transform," Opt. Laser Technol. **37**(6), 458–462 (2005).
10. U. Schnars and W. Jüptner, "Direct Recording of Holograms by a CCD Target and Numerical Reconstruction," Appl. Opt. **33**(2), 179–181 (1994).
11. E. Cuche, F. Bevilacqua, and C. Depeursinge, "Digital Holography for Quantitative Phase Contrast Imaging," Opt. Lett. **24**(5), 291–293 (1999).
12. X. Chen, C. Tang, W. Xu, Y. Su, and K. Su, "General construction of transform-domain filters, filtering methods for electronic speckle pattern interferometry, and comparative analyses," Appl. Opt. **55**(9), 2214–2222 (2016).
13. A. Frederico and G. H. Kaufmann, "Comparative study of wavelet thresholding methods for denoising electronic speckle pattern interferometry fringes," Opt. Eng. **40**(11), 2598–2604 (2001).
14. T. Asakura, "Surface roughness measurements," in *Speckle Metrology*, R. K. Erf, ed., pp. 11–49 (Academic Press, New York, 1978).

15. Z. Wang, A. C. Bovik, and L. Lu, "Why is image quality assessment so difficult?" Proc. IEEE ICASSP **4**, 3313–3316 (2002).
16. A. Federico and G. H. Kaufmann, "Denoising in digital speckle pattern interferometry using wave atoms," Opt. Lett. **32**(10), 1232–1234 (2007).
17. P. Memmolo, I. Esnaola, A. Finizio, M. Paturzo, P. Ferraro, and A. M. Tulino, "SPADEDH: a sparsity-based denoising method of digital holograms without knowing the noise statistics," Opt. Express **20**(15), 17250–17257 (2012).
18. T. Baumbach, E. Kolenovic, V. Kebbel, and W. Jüptner, "Improvement of accuracy in digital holography by use of multiple holograms," Appl. Opt. **45**(24), 6077–6085 (2006).
19. L. Rong, W. Xiao, F. Pan, S. Liu, and R. Li, "Speckle noise reduction in digital holography by use of multiple polarization holograms," Chin. Opt. Lett. **8**(7), 653–655 (2010).
20. V. Bianco, M. Paturzo, P. Memmolo, A. Finizio, P. Ferraro, and B. Javidi, "Random resampling masks: a non-Bayesian one-shot strategy for noise reduction in digital holography," Opt. Lett. **38**(5), 619–621 (2013).
21. R. C. Gonzales and R. E. Woods, *Digital Image Processing*, 3rd ed. (Prentice Hall, Upper Saddle River, 2008).
22. J. S. Lee, ""Digital image enhancement and noise filtering by using local statistics," IEEE Trans. on Patt," Anal. And Mach. Intell. **2**, 165–1658 (1980).
23. V. S. Frost, J. A. Stiles, K. S. Shanmugan, and J. C. Holtzman, "A model for radar images and its application to adaptive digital filtering of multiplicative noise," IEEE Trans. Patt. Anal. And Mach. Intell PAMI **4**(2), 157–166 (1982).
24. S. Mallat, *A Wavelet Tour of Signal Processing* (Academic Press, New York, 1999).
25. D. L. Donoho, "De-noising by soft-thresholding," IEEE Trans. Inf. Theory **41**(3), 613–627 (1995).
26. H. Xie, L. E. Pierce, and F. T. Ulaby, "Sar speckle reduction using wavelet denoising and markov random field modeling," IEEE Trans. Geosci. Rem. Sens. **40**(10), 2196–2212 (2002).
27. J.-L. Starck, E. J. Candès, and D. L. Donoho, "The curvelet transform for image denoising," IEEE Trans. Image Process. **11**(6), 670–684 (2002).
28. M. N. Do and M. Vetterli, "The contourlet transform: an efficient directional multiresolution image representation," IEEE Trans. Image Process. **14**(12), 2091–2106 (2005).
29. G. H. Kaufmann and G. E. Galizzi, "Speckle noise reduction in television holography fringes using wavelet thresholding," Opt. Eng. **35**(1), 9–14 (1996).
30. A. A. Shulev, A. Gotchev, A. Foi, and I. R. Roussev, "Threshold selection in transform-domain denoising of speckle pattern fringes," Proc. SPIE **6252**, 625220 (2006).
31. A. Buades, B. Coll, and J. M. Morel, "A review of image denoising algorithms, with a new one," Multiscale Model. Simul. **4**(2), 490–530 (2005).
32. A. Buades, B. Coll, and J. Morel, "A non-local algorithm for image denoising," Proc. IEEE Comput. Soc. Conf. Comput. Vis. Pattern Recognit. **2**(2), 60–65 (2005).
33. A. Uzan, Y. Rivenson, and A. Stern, "Speckle denoising in digital holography by nonlocal means filtering," Appl. Opt. **52**(1), A195–A200 (2013).
34. K. Dabov, A. Foi, V. Katkovnik, and K. Egiazarian, "Image denoising with block-matching and 3D filtering," Proc. SPIE **6064**, 606414 (2006).
35. K. Dabov, A. Foi, V. Katkovnik, and K. Egiazarian, "Image denoising by sparse 3-D transform-domain collaborative filtering," IEEE Trans. Image Process. **16**(8), 2080–2095 (2007).
36. V. Katkovnik, A. Foi, K. Egiazarian, and J. Astola, "From local kernel to nonlocal multiple-model image denoising," Int. J. Comput. Vis. **86**(1), 1–32 (2010).
37. Q. Kemao, "Windowed Fourier transform for fringe pattern analysis," Appl. Opt. **43**(13), 2695–2702 (2004).
38. L. Huang, Q. Kemao, B. Pan, and A. Asundi, "Comparison of Fourier transform, windowed Fourier transform, and wavelet transform methods for phase extraction from a single fringe pattern in fringe projection profilometry," Opt. Lasers Eng. **48**(2), 141–148 (2010).
39. Q. Kemao, T. H. Nam, L. Feng, and S. H. Soon, "Comparative analysis on some filters for wrapped phase maps," Appl. Opt. **46**(30), 7412–7418 (2007).
40. Q. Kemao, "On window size selection in the windowed Fourier ridges algorithm," Opt. Lasers Eng. **45**(12), 1186–1192 (2007).
41. Q. Kemao, "Two-dimensional windowed Fourier transform for fringe pattern analysis: Principles, applications and implementations," Opt. Lasers Eng. **45**(2), 304–317 (2007).
42. P. Memmolo, M. Iannone, M. Ventre, P. A. Netti, A. Finizio, M. Paturzo, and P. Ferraro, "Quantitative phase maps denoising of long holographic sequences by using SPADEDH algorithm," Appl. Opt. **52**(7), 1453–1460 (2013).
43. V. Bianco, P. Memmolo, M. Paturzo, A. Finizio, B. Javidi and P. Ferraro, "Quasi noise-free digital holography," Light Science & Applications, accepted article preview 31 March 2016.
44. M. Karray, P. Slangen, and P. Picart, "Comparison between digital Fresnel holography and digital image-plane holography: the role of the imaging aperture," Exp. Mech. **52**(9), 1275–1286 (2012).

1. Introduction

Digital holography is an effective and robust method for imaging and metrology [1,2]. Holographic phase imaging measures the optical path length map associated with transparent specimens (transmission illumination) or opaque surfaces (reflection illumination) and translates this data into relevant information. The measured field of interest is related to a

wrapped modulo 2π phase map (also called phase fringe pattern). A limitation of digital holographic phase imaging is related to speckle decorrelation which occurs between two consecutive temporally varying digital holograms [3–5]. Note that in digital holography, the phase decorrelation noise may have several origins [4]. The direct consequence is that this decorrelation adds a high spatial frequency noise to the useful phase data. Then, robust noise filtering has to be implemented in order to yield measured phase fringe patterns suitable for quantitative measurement. Usually, and in order to preserve the 2π phase jump in the wrapped phase map, phase processing is carried out on the sine and cosine images calculated from the raw phase [6,7]. At the final step, the processed phase map has to be unwrapped in order to get a quantitative measurement of the measurand of interest (displacement, field, strain field, vibration field, etc…) with a robust noise immune algorithm [8,9]. Note that unwrapping will be not discussed in the paper. In this paper we aim at comparing the performances of different advanced algorithms for phase data de-noising. In order to quantify the performances, four criteria are proposed. These criteria are the gain in the signal-to-noise ratio, the Q index, the standard deviation of the phase error, and the signal to distortion ratio. As a general rule, experimental data cannot provide a comparison with an exact expected value. Then, the methodology we propose to investigate the de-noising algorithms is based on the use of a realistic simulation of noise-corrupted phase data, to apply de-noising on sine/cosine images of phase, and to use the above mentioned criteria to qualify the methods.

This paper is organized as follows; in section 2, we describe the theoretical basics and the phase decorrelation noise in the phase measurement; section 3 discusses on the realistic simulation of corrupted phase. In section 4, the criteria to qualify the performances of algorithms are presented. Section 5 provides details on the de-noising algorithms considered for the study. In Section 6, the results of the benchmark are presented and discussed, and rankings of the methods are given. Section 7 proposes application of the best de-noising method to experimental data. Conclusions and perspectives to the study are drawn in section 8.

2. Basics of digital Fresnel holography

A digital hologram is obtained by recording with a pixel matrix sensor the coherent mixing of a so-called object wave (O) and a so-called reference wave (R). The hologram is usually written as [1,2,10,11]:

$$H = |R|^2 + |O|^2 + R^*O + RO^*. \tag{1}$$

In Eq. (1), the reference wave is generally written $R(x,y) = a_R\exp[2i\pi(u_0 x + v_0 y)]$ with spatial frequencies $\{u_0,v_0\}$ (off-axis configuration), and O is the wave diffracted in the recording plane by the object located at distance d_0 from this plane. The object wave O can be expressed under the Fresnel approximations by Eq. (2) [1,2,10,11] ($i = \sqrt{-1}$):

$$O(x,y,d_0) = -\frac{i}{\lambda d_0}\exp\left(\frac{2i\pi d_0}{\lambda}\right)\exp\left(\frac{i\pi}{\lambda d_0}\left(x^2 + y^2\right)\right)$$
$$\times \iint A(X,Y)\exp\left(\frac{i\pi}{\lambda d_0}\left(X^2 + Y^2\right)\right)\exp\left(-\frac{2i\pi}{\lambda d_0}(xX + yY)\right)dXdY. \tag{2}$$

The object wave front at the object plane is $A(X,Y) = A_0(X,Y)\exp[i\psi_0(X,Y)]$ and λ is the wavelength of light. The reconstruction of the object field at distance $-d_0$ from the recording plane is given by the discrete Fresnel transform [10]:

$$A_r(X,Y,-d_0) = \frac{i\exp(-2i\pi d_0/\lambda)}{\lambda d_0}\exp\left[-\frac{i\pi}{\lambda d_0}\left(X^2 + Y^2\right)\right]$$
$$\times \sum_k\sum_l H(lp_x,kp_y,d_0)\exp\left[-\frac{i\pi}{\lambda d_0}\left(l^2 p_x^2 + k^2 p_y^2\right)\right]\exp\left[\frac{2i\pi}{\lambda d_0}(lXp_x + kYp_y)\right]. \tag{3}$$

Equation (3) includes the pixel coordinates (lp_x, kp_y) at which the digital hologram is recorded (l, k: integers; p_x, p_y: pixel pitches). From the numerical computation, the amplitude and phase of the diffracted field can be evaluated. As a general rule, and except for digital holographic microscopy, the object wave front is speckled. Quantitative measurement is carried out by a subtraction between the object phase and a "reference" phase, the reference being that of the object at the so-called "reference" state. The obtained phase difference is given modulo 2π and phase unwrapping is then required [8]. This approach is limited by the speckle phase decorrelation which occurs between the two states of the object. This decorrelation noise may have several origins: modifications at the object surface (due to loading such as mechanical, vibrations, heating, pneumatic,…), laser wavelength change between exposures (e.g. surface shape measurement), reduced number of recording pixels (low resolution of the sensor), defocusing of the reconstructed image (the reconstruction distance is "not good"), saturation of the recorded hologram, quantization effect due to a low number of useful bits or shot-noise if the number of photo-electrons is too low. In speckle metrology, the decorrelation noise due to modifications at the object surface is the main contribution to noise and its contribution to the noise standard deviation is much larger than the other error sources. The speckle phase decorrelation noise is related to the correlation property of the two speckle fields given at the two object states. This correlation property is related to the second-order probability density function of the phase [3]. Here, we note ε the noise induced by the speckle decorrelation between two object fields (with phases ψ_1 and ψ_2) reconstructed for two different states and $\Delta\varphi$ the phase change due to the modifications at the object surface. Then we have $\psi_2 = \psi_1 + \varepsilon + \Delta\varphi$, and phase change $\Delta\varphi$ is considered as deterministic. The probability density function of phase noise ε depends on the modulus of the complex coherence factor $|\mu|$ between the two speckle fields. Parameter $|\mu|$ indicates the correlation between the two speckle fields. If $|\mu| = 0$, the fields are not correlated and their phase difference is uniformly distributed over range $[-\pi, +\pi]$, thus noise is high. If $|\mu| = 1$, the fields are fully correlated and the phase difference is close to 0, thus noise is weak. With $\beta = |\mu|\cos(\varepsilon)$, the second-order probability density of the phase noise ε is given by [3,5]:

$$p(\varepsilon) = \frac{1-|\mu|^2}{2\pi}\left(1-\beta^2\right)^{-3/2}\left(\beta\sin^{-1}\beta + \frac{\pi\beta}{2} + \sqrt{1-\beta^2}\right). \tag{4}$$

This probability density is centered (mean value at 0) and its width depends on $|\mu|$. Curves of Eq. (4) versus $|\mu|$ are given in Fig. 1.
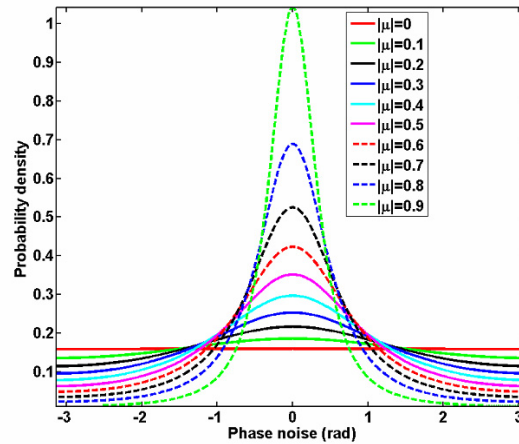

Fig. 1. plots of the probability density function vs different values of $|\mu|$.

When the coherence factor increases, the probability density tends to be narrower, and for value of $|\mu|>0.99$, it can be considered as quasi-Gaussian. However, for $|\mu|<0.99$, the probability density is not Gaussian, and this means that the decorrelation phase noise cannot be assimilated to a Gaussian white noise. In addition, the decorrelation noise is closely related to the fringes produced by the object surface changes. When surface changes produce more and more fringes, then decorrelation phase noise increase and the signal-to-noise ratio (SNR) decreases strongly. It follows that SNR is related to the fringe number. This means that evaluation of filtering method for speckled phase images cannot be carried out by considering a simple Gaussian additive noise, as was proposed in ref [7,9,12]. Indeed, it would be not realistic to add Gaussian noise to any phase map to simulate decorrelation noise, and simply adjusting the SNR level by adjusting the standard deviation of the added Gaussian noise. In order to take into account this close link between fringe density and SNR, a realistic simulation has to be implemented.

3. Realistic simulation of corrupted phase data

3.1 Principle

In order to evaluate the performances of de-noising and restoration, a realistic numerical simulation was developed. The goal of the simulation is to produce phase map corrupted by speckle decorrelation noise with the adequate probability density function. In experiments, the amount of speckle phase decorrelation is naturally controlled by the fringe density, which is related to the surface modifications. The larger the surface deformation, the higher the number of fringes, and hence the higher the phase decorrelation between the two states of the object surface. Several authors proposed a scheme to simulate speckle interferometry fringes [13,14]. In these previous works, the intensity distribution is of primary interest. In this paper, we aim at simulating phase decorrelation effects that corrupt the digital modulo 2π fringes. The arrangement to produce speckle phase decorrelation is given Fig. 2. The surface is supposed to be rough compared to the wavelength of light (visible range) and is illuminated by a uniform plane wave. The two lenses have the same focal length (f), and a circular diaphragm with radius R_u is inserted in the back focal plane of the first lens (i.e. the Fourier plane of the 4-f optical system). If $A(x,y) = A_0\exp(i\varphi_0)\delta(x-x_0,y-y_0)$ (δ is the Dirac delta function) is the complex field of a single point in the object plane localized at (x_0,y_0), then the corresponding complex amplitude at the image point is given by the convolution equation according to $A'(X,Y) = A(X,Y)*PSF(X,Y)$ (* means convolution) with PSF being the point spread function given by Eq. (5) [13]:

$$PSF(X,Y) = -\frac{i}{\lambda f}\exp\left(\frac{2i\pi f}{\lambda}\right)\exp\left(\frac{i\pi}{\lambda f}\left(X^2 + Y^2\right)\right)$$
$$\times \iint p(x',y')\exp\left(-\frac{2i\pi}{\lambda f}(x'X + y'Y)\right)dx'dy'. \tag{5}$$

In Eq. (5), $p(x',y')$ is the pupil function provided by the diaphragm in the back focal plane, i.e. $p(x',y') = 1$ if $x'^2 + y'^2 \leq R_u^2$ and 0 elsewhere. The value of R_u is adjusted to control the speckle grain size in the image plane and to simulate realistic images. From a practical point of view, the convolution equation can be carried out with two-dimensional fast Fourier transforms. The roughness is numerically simulated by considering a surface profile $h(x,y)$ with roughness having Gaussian statistics and has a Dirac delta autocorrelation function. This random surface generates a random optical phase $\psi = 2\pi h/\lambda$. The surface deformation is simulated by using an analytical model, such as Gaussian distribution, first, second and third order polynomials, and Matlab function "membrane". The surface deformation is then added to the surface roughness.

In order to get phase change due to surface deformation and including speckle phase decorrelation, the procedure is as follows: first calculate the convolution equation with the random surface to produce a random "reference" speckle field in the image plane, second

calculate the convolution equation with the random surface to which is added the surface deformation to produce a random "deformed" speckle field in the image plane, last calculate the phase difference between the two previous speckle phases from the two calculated optical fields. Phase decorrelation occurs because of the spatial filtering produced by the diaphragm in the back focal plane. Note that the signal-to-noise ratio obtained in the phase difference image is related to the speckle noise and the amplitude of the deformation. As a result, the speckle phase decorrelation noise follows the same statistics as given in Eq. (4).

In order to illustrate few outputs of the simulation process, Fig. 3 shows data obtained with an image size at 1024 × 1024 pixels, pixel pitch at $p_x = 5\mu m$, $\lambda = 632.8nm$, and speckle grain at 20μm. The size of the speckle grain is estimated by calculating the autocorrelation of the speckle intensity in the image plane. Figure 3(a) shows the surface deformation given in radians and used for input in the convolution calculation. Figure 3(b) shows the modulo 2π noisy phase difference that is obtained by subtracting the two phases from the two calculated optical fields. It can be seen that it includes the speckle phase decorrelation noise. Figure 3(c) exhibit the autocorrelation of the speckle intensity providing the size of the speckle grain (in this case grain size is at 20μm). Figure 3(d) gives the decorrelation noise calculated by subtracting the initial simulated modulo 2π deformation with the noisy modulo 2π phase map.
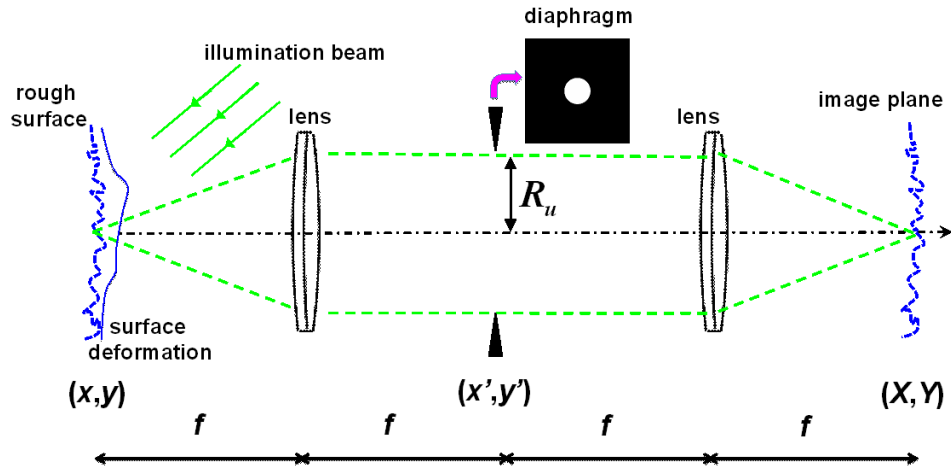

Fig. 2. Arrangement to produce speckle phase decorrelation in phase change due to surface deformation.

From the noise map of Fig. 3(d), the probability density of the decorrelation noise can be estimated. In Fig. 3(e), the red curve shows the probability density obtained from theory (Eq. (4)) after least square fitting, and the blue curve shows that obtained from Fig. 3(d). Finally Fig. 3(f) shows the cosine image of the noisy phase for which the signal-to-noise ratio (SNR) is estimated at 5.09dB. From the estimated probability density of the decorrelation noise in Fig. 3(e), the fit with Eq. (4) leads to the coherence factor $|\mu|$. In this example, it is estimated to $|\mu| = 0.915$, and the standard deviation of the decorrelation phase noise is $\sigma = 0.657rad$. Figures 3(b) and 3(e) shows that the noise simulation is quite realistic and corresponds to what is observed in real experiments. Note that the coherence factor can be used as a quality marker for the measurement in high-speed holographic interferometry [4,5].
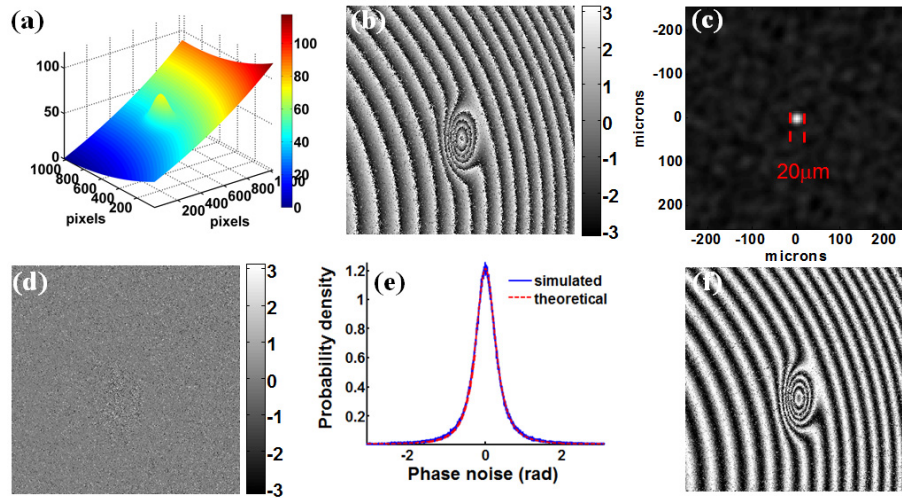
Fig. 3. Examples of outputs from the numerical simulation, (a) surface deformation in radians, (b) modulo 2π noisy phase map including the speckle phase decorrelation, (c) autocorrelation of the speckle intensity providing the size of the speckle grain, (d) decorrelation noise, (e) probability density of the decorrelation noise (red: theoretical Eq. (4), blue: obtained from Fig. 3(d), and 3(f) cosine image of the noisy phase, the signal-to-noise ratio in this image is 5.08dB.

3.2 Database for benchmark

The database for the benchmark consists of simulated fringe images in which the type of the fringe pattern and the noise level are controlled. The use of several fringe pattern permits to consider a certain "fringe diversity" so as to establish statistics on the obtained results. For this purpose, we chose five different fringe patterns. In addition, five values for the SNR were simulated by decreasing the SNR value with adding to the simulation a wavelength change. This helps to simulated degraded phase images according to real experimental conditions for which a lot of limiting factors may influence the quality of the measurement [5]. The five SNR values are 7.31dB, 6.10dB, 5.08dB, 4.03dB and 3.10dB, respectively for the five rows. Figure 4 shows for one of the fringe pattern, the set of data for the five SNR values. For a given SNR, each row shows respectively the cosine of the noisy phase (Figs. 4(a), 4(f), 4(k), 4(p), 4(u)), the sine of the noisy phase (Figs. 4(b), 4(g), 4(l), 4(q), 4(v)), the modulo 2π deformation phase maps (Figs. 4(c), 4(h), 4(m), 4(r), 4(w)), the modulo 2π noisy deformation phase maps (Figs. 4(d), 4(i), 4(n), 4(s), 4(x)), and the the noise maps extracted from the simulation (Figs. 4(e), 4(j), 4(o), 4(t), 4(y)).

Figure 5 shows the 5 fringe patterns of the set of data for one SNR value. Figures 5(a)–5(e) show the cosine of the simulated deformation phase. Figures 5(f)–5(j) show the cosine of the noisy deformation phase for SNR at respectively 3.10dB, 3.59dB, 3.34dB, 3.66dB and 3.65 dB, thus an average value at 3.46dB. Figures 5(k)–5(o) show the simulated modulo 2π deformation phase maps. In Figs. 5(p)–5(t) the modulo 2π noisy deformation phase maps are exhibited. Last, Figs. 5(u)–5(y) show the noise maps extracted from the simulation.
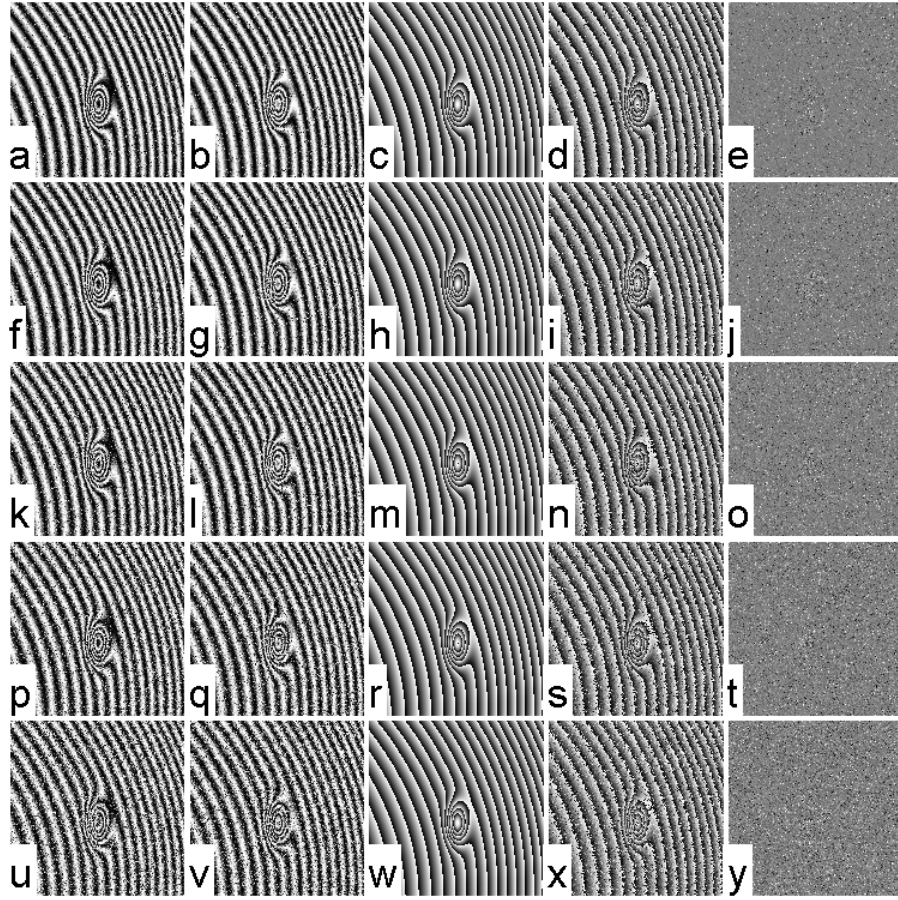
Fig. 4. Outputs from the numerical simulation for 5 different values of the SNR, respectively for each row at 7.31dB, 6.10dB, 5.08dB, 4.03dB and 3.10dB, (a),(f),(k),(p),(u) respectively the cosine of the noisy phase, (b),(g),(l),(q),(v) the sine of the noisy phase, (c),(h),(m),(r),(w) the modulo 2π deformation phase maps, (d),(i),(n),(s),(x) the modulo 2π noisy deformation phase maps, and (e),(j),(o),(t),(y) the noise maps extracted from the simulation.
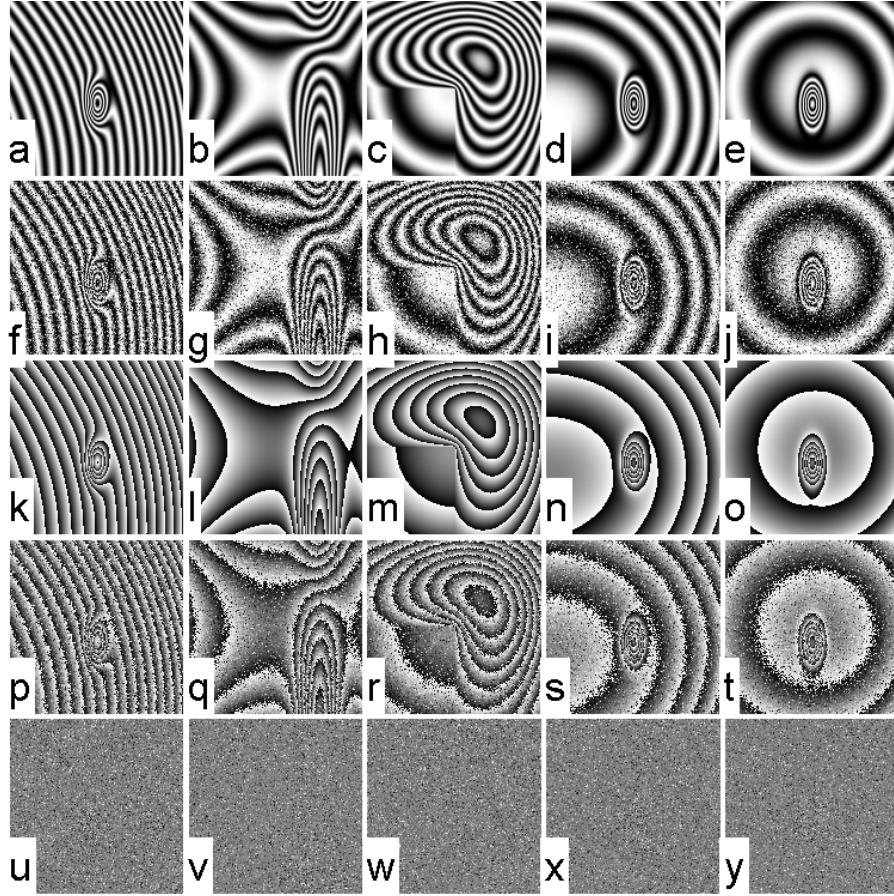
Fig. 5. Outputs from the numerical simulation for 5 different fringe patterns, (a) to (e): cosine of the simulated phase, (f) to (j): cosine of the noisy phase for SNR at respectively 3.10dB, 3.59dB, 3.34dB, 3.66dB and 3.65 dB (average value at 3.46dB), (k) to (o): simulated modulo 2π deformation phase maps, (p) to (t): modulo 2π noisy deformation phase maps, (u) to (y): noise maps.

The next section discusses on the evaluation criteria which were used to rank the different de-noising methods discussed in section 5.

4. Evaluation criteria

The de-noising methods are used to enhance the phase difference and to reduce the speckle decorrelation noise. As a general rule, the filtering is not applied on the raw modulo 2π phase because the phase jumps must be preserved. Thus, de-noising is applied on the sine and cosine images of the raw phase, and the enhanced modulo 2π phase is calculated by an arctangent formula; by this way filtering does not destroy the phase jumps which are of primary interest to unwrap the phase. For each test in the benchmark, four evaluation criteria are computed. The first one is the gain in the SNR provided by the de-noising method. Given the importance of cosine and sine images in the restoration process, the gain is calculated from the estimated SNR of the cosine and sine images of the phase. The gain in the SNR is defined according to Eq. (6):

$$G_{SNR} = R_{SNR} - I_{SNR}. \tag{6}$$

In Eq. (6), R_{SNR} and I_{SNR} are respectively the SNR measured at the output and at the input of the de-noising processing, and its value is given in dB unit. The residual SNR, noted R_{SNR}, is defined from the original noise-free image $s(i,j)$ and the de-noised image $d(i,j)$ according to:

$$R_{SNR} = 10 \log_{10} \left[\frac{\sum\limits_{i,j} s^2(i,j)}{\sum\limits_{i,j} \left[s(i,j) - d(i,j) \right]^2} \right]. \tag{7}$$

As a general rule, the SNR and its variants are intensively used to evaluate methods of image enhancement and restoration. However, such criterion has a significant drawback since it is based on the calculation of an average error which does not account for distortions which may affect the structures in the image. Thus, the same amount of error can be observed between two images restored for an image having a very different perceived quality. In order to address this drawback, Wang and Bovik proposed what they called the "quality index" criterion [15]. This criterion has the property of better exhibiting the quality of the perceived image. Equation (8) gives the useful expression to calculate the quality index:

$$Q_{index} = \frac{\sigma_{sd}}{\sigma_s \sigma_d} \frac{2\mu_s \mu_d}{\mu_s^2 + \mu_d^2} \frac{2\sigma_s \sigma_d}{\sigma_s^2 + \sigma_d^2}. \tag{8}$$

In Eq. (8), μ_s and μ_d are the mean values of images $s(i,j)$ and $d(i,j)$, σ_s and σ_d are their variances and σ_{sd} their covariance. The value of Q_{index} is included in the interval $[-1, +1]$, the latter being reached when the two images are quite similar. Note that this criterion was also considered by Federico and Kaufmann in their work about de-noising speckle interferogram using wave atoms [16]. The third criterion is related to the error on the phase reconstruction. Indeed, the main goal of the phase measurement is related to metrology purpose, and then the phase error is an important parameter of the de-nosing method. The phase error is calculated by subtracting the original simulated phase deformation to the de-noised phase, and then the standard deviation σ_φ is estimated according to Eq. (9):

$$\sigma_\phi = \sqrt{\left\langle \varepsilon_\phi^2 \right\rangle - \left\langle \varepsilon_\phi \right\rangle^2}. \tag{9}$$

In Eq. (9), $\varepsilon_\varphi = \Delta\varphi_s - \Delta\varphi_f$, $\Delta\varphi_f$ is the enhanced phase difference and $\Delta\varphi_s$ is the initial noise-free simulated phase. The last criterion that is considered in this paper is the signal to distortion ratio (SDR) [17] defined by:

$$SDR = \frac{\|s\|_2}{\|s - d\|_2}. \tag{10}$$

In Eq. (10), $\|...\|_2$ means l_2 norm. Note that to apply Eq. (10) we consider image s being the initial noisy image (and not the initial noise free image, as for the other criteria). The reason is that we aim also at comparing criteria that could be applied in the absence of information about noise, as it is mainly the case for real data sets. Note that the speckle contrast defined in [18–20] could be also considered. However, this criterion is not applicable to modulo 2π phase maps because it is too much sensitive to phase jumps. Thus, the speckle contrast will be not considered in this paper. The next section describes the de-noising processes which were considered in this study.

5. Methods and algorithms for speckle reduction

5.1 Spatial filtering

Spatial filtering is the most commonly applied filtering in digital speckle pattern interferometry [6,7]. To preserve the phase jumps, it is applied on the sine and cosine of the phase. Several types of kernels can be considered: the moving average filter (not considered here), the median filter (efficient for impulsive noise) or the Gaussian filter. The size of the kernel may vary from 3 × 3 to 21 × 21 for images at 512 × 512 or 1024 × 1024 pixels. These filters are generally very easy to implement and they constitute reference methods to evaluate other more complex algorithms.

5.2 Wiener filtering

The Wiener deconvolution is a mathematical operation applying a filter to eliminate the noise in any signal. This filtering operates in the frequency domain by trying to minimize the impact of noise where the SNR is bad. From a mathematical point of view, this is the solution, in the least square sense, of the minimization of the mean square error computed between the original image $s(x,y)$ and the filtered image $d(x,y)$, in case of linear spreading model with additive noise $b(x,y)$. According to [21], the transfer function of the Wiener filter, $W(u,v)$, is given by Eq. (11):

$$W(u,v) = \frac{H(u,v)\Phi_s(u,v)}{|H(u,v)|^2 \Phi_s(u,v) + \Phi_b(u,v)}. \tag{11}$$

In Eq. (11) the spreading function $H(u,v)$ can be chosen to be unitary, Φ_s is the estimated power spectrum density of the original image and Φ_b is the estimated power spectrum density of noise. The power spectrum densities of original image and noise are not known a priori. The median filtering is applied on the noisy image to get estimations of both the noise and the original image. The original image is simply estimated by applying the median filtering on the noisy image. Noise is estimated by calculating the difference between the raw noisy image and the median filtered noisy image.

5.3 SAR filtering

Synthetic Aperture Radar (SAR) filtering can be applied to speckle images, because intrinsically SAR images include same properties as that of speckle images, the noise model being considered as multiplicative. Lee proposed an adaptive filter [22] is which the parameters are adapted according to the local statistical properties of the image to be processed. These parameters are estimated in a window centered on the pixel for which one expects restoring the correct value. Computation of the filtering can be described by Eq. (12):

$$d(x,y) = \alpha\, s(x,y) + (1 - \alpha\mu_s). \tag{12}$$

Parameter $\alpha = 1 - C_b^2/C_s^2$ depends on the ratio of the squares of the local variation coefficients of the image, C_s, and noise, C_b. This local variation coefficient is defined as the ratio of the variance between the mean square of the considered pixel values. In a region with homogeneous values, the local variation coefficient is low (≈ 0), and the filter does not modify the image. In the opposite case, if this variation is larger than that of the noise, the current value of the pixel is considered. An alternative approach was proposed by Frost [23]. The filter consists in an adaptive Gaussian filter kernel. The kernel parameters are adjusted according to the local statistics of the image by considering the local variation coefficient C_s^2. In the presence of an edge or a discontinuity, the coefficient increases and the Gaussian kernel is concentrated around the current pixel, ultimately its original value is retained. In a region with homogeneous values, the local variation coefficient is low (≈ 0), and the filter behaves as a simple averaging. If the variation in the observed image is less than that of the noise, α is equal to 0, and the average of the window is affected at the value of the pixel.

5.4 Wavelet thresholding approaches

Image enhancement can also be considered in the sense of a decomposition on a wavelet basis associated with a threshold function [24,25]. The basic idea is to apply a threshold operator on the wavelet coefficients computed from the image to be restored. If the wavelet basis is adapted to the signal contents, its representation in the wavelet coefficients space is sparse. This means that the highest coefficients concentrate information about the image. Then, applying a threshold leads to leave off the least significant coefficients which are supposed to be related to the noise. In such an approach, the model considers an additive noise. Using the wavelet transformation, the same process is applied to the coefficients. When the noise is not additive but multiplicative, additive signal and noise are obtained by computing the

logarithm. This was studied in the case of speckle noise processing in SAR images [26]. Multiple variants of solutions, not detailed here, are available by adjusting many parameters of this method: choice of the wavelet basis, number of decomposition levels, profile of the thresholding operator, threshold values and their different associated estimator. In this benchmark, we consider separable wavelets *Daubechies* and *symlets* builds from the tensor product of their one dimensional release, *curvelets* and *contourlets* [27,28] built in a circular paving plane, thus offering a wide range of orientation waveforms. Note that such an approach was applied to the de-noising of noisy speckle interferograms [16,29,30].

5.5 Non-local means method

Non local means method (NL-means) were recently proposed [31,32]. It constitutes an efficient technique for the enhancement of images corrupted by additive noise. The principle is to consider the pixel value replacement by a weighted sum of values included in patches that are chosen in the neighborhood of the pixel to be processed. The weighting is obtained from correlations estimated between the local patch of the pixel to be processed and the patch of the neighborhood patches that are taken into account in the algorithm. Thus, when a patch is strongly correlated with the local patch of the pixel to be processed, the pixel is taken into account in the weighting with a coefficient evaluated from a Gaussian kernel which argument is the Euclidean distance between the two patches. Such method was already used with success for speckle images from digital holography but with a different methodology approach (blind criterion without a reference image) [33]. In addition, the processing of the phase was not considered in this previous study.

5.6 BM3D method

Since its introduction by Dabov [34,35], the transform-based block-matching 3-D (BM3D) filter is recognized as state-of-the art in image de-noising. The important point to address is that BM3D filter combines various efficient techniques and synthesizes major advances that have occurred in recent years [36]. Among them, the approaches based on the decomposition of the image in patches, like NL-means method [31] and the use of shrinkage operators applied on image transform domain as wavelet representations. The BM3D filter exploits a particular nonlocal image modelling through a procedure termed grouping and collaborative filtering. Grouping finds mutually similar 2-D image blocks and stacks them together in 3-D arrays. Collaborative filtering produces individual estimates of all grouped blocks by filtering them jointly, using transform-domain shrinkage operator of the 3-D arrays. BM3D relies both on local and non-local characteristics of images. It follows the presence of numerous similar patches and that the image is locally highly correlated. When these assumptions are verified, a sparse representation of the group is obtained by applying a decorrelation 3-D transform. Due to the particular structure of interference fringe images which are regular and contain no complex textures, these assumptions remain true. The sparsity of the true image determines the success of the shrinkage operator to separate the noise from the observation and it means that its energy is compactly represented in the 3-D transform domain. The previous described operations constitute in fact the first stage of the overall method. Estimated true image is then used to perform in a second stage a Wiener like filtering onto the coefficients of the 3-D transform of similar stacked patch group. As a final stage, an aggregation procedure is performed on estimated true patches in order to compute the resulting value of pixels by summing patches using a weighting in a similar way as uses the NL-means method. The BM3D algorithm is based on the optimization of a very large number of parameters, at least a dozen. So, it is difficult to measure the impact of various components separately. For this reason, we have kept the parameters suggested by authors in the given software [34].

5.7 2-D windowed Fourier transform filtering

The 2-D windowed Fourier transform filter (WFT2F) method [37,38] is based on a local Fourier transform (FT) which can takes into account the non-stationary characteristics of the speckle noise. So, frequency components of a fringe pattern can be extracted from noise with

more accurate efficiency than with a FT computed overall phase maps, as acts, for example, the Wiener filter method. In a similar way than for wavelet transforms, but adapted to a complex representation, the filtering process consists in applying a threshold to the modulus of the 2-D Fourier coefficients, letting the phase unchanged. Finally, an inverse 2-D windowed Fourier transform (IWFT2F) of the filtered frequency domain is then computed to get the modulo 2π phase of the fringe pattern. The WFT2F can be seen as a projection of the phase map onto 2-D oscillating functions which are localized in the spatial and the frequency domain. The discrete version of this algorithm leads to setting eight parameters, defining the window size, the threshold value and six parameters for sampling of the frequency axis. For the quantitative appraisal, we have keep values proposed by the author [39–41] which seems to be well adapted to the processing of phase fringe patterns.

5.8 SPADEDH algorithm

SPADEDH algorithm was proposed by Memmolo in reference [17], and means SPArsity DEnoising of Digital Holograms. This approach considers l_1 minimization algorithm and is able to suppress the noise components on digital holograms without any prior knowledge or estimation about the statistics of noise. It was applied to noisy phase maps with Gaussian statistics [42]. During last decade compressive sensing (CS) approaches have brought major improvements in many fields of applications including signal processing stages. CS appears as a new paradigm of sampling theory in which samples are not anymore resulting from the acquisition along a regular grid of the quantity to record but from a projection onto an operator in which the signal is sparsely represented. In order to select the coefficients from the representation, a sparsity measure associated to a selection algorithm must be applied. L_0 and L_1 norms have been shown to be the appropriate measures. In certain conditions, L_0 and L_1 norms lead to the same solutions. There exist also two main families of selection algorithms: greedy and minimization algorithms. The SPADEDH algorithm is based on a greedy approach which is the stagewise orthogonal matching pursuit. This algorithm is able to suppress the noise components on digital holograms without any prior knowledge or estimation about the statistics of noise. It was applied to noisy phase maps with Gaussian statistics [43].

Note that other efficient de-noising approaches were proposed in the field of digital holography. They are based on multi-look digital holography [18,19] which addresses the problem by reducing the light coherence by engineering the laser source or by recording and incoherently combining multiple holograms after providing some type of noise decorrelation between the captured data. For example, in [43], this approach is combined to BM3D algorithms to substantially enhance the reconstructed color holographic images. In the context of this study, this approach cannot be applied because we aim at considering de-noising performances by using a single noisy fringe map. In addition, applying this approach to multiple phase maps supposes that one is able to perfectly reproduce the surface deformation between the non-correlated sets of holographic recordings.

6. Results and discussions

For the evaluations, we selected a total of 34 algorithms differentiated by the used methods and their parameters. These methods are listed hereafter. The linear filter method with a Gaussian kernel sized 3×3 and 5×5 was taken into account. The median filter was used with kernel from 3×3 to 21×21 (7 odd mask sizes). The method of Wiener filtering was used with a unique setting. The Lee filter has no parameter, but the Frost filter was used with the same sizes as the median filter. The NLmeans method was considered with three sets of parameters (5,7,30), (5,11,40) and (7,15,30), which respectively represent the size of the patch, the size of the neighborhood to search for similar patches, and the declining value of the Gaussian kernel used for computation of distances between patches. For stationary wavelet, Daubechies and symlets were used with five and three values of the regularity parameter (1,3,4,6,8) and (4,6,8). Note that for these two last algorithms, the decompositions are performed on three levels with a hard thresholding applied to the non-decimated detail

coefficients that are calculated for each level. Last, we considered decompositions with curvelet, contourlets, BM3D and WFT2F for which we have kept the parameters of the algorithms provided by their respective authors. Finally, we considered the SPADEDH algorithm which has no parameter.

Each method was evaluated by four values representing the average of the four indices Q_{index}, G_{SNR}, σ_φ, and *SDR* (see section 4) with the 25 images of simulated phases from the database. These 25 images represent five different fringe shapes and densities, and five different SNR of the cosine image, the SNR being in the range [3dB, 11dB] (see Fig. 4 and Fig. 5).

Figure 6 summarizes the results obtained for the four indices by presenting their ranking. For better conciseness, 20 results were selected for which, whenever it was possible, the set of parameters offered the best results. However, all the methods discussed in section 5 are represented in the paper. The height of the vertical color bars represents values of averaged values over the entire database. We also represent, within each index bar, a second bar of different color corresponding to the standard deviation associated with the values displayed for the entire database.

Figure 6(a) shows the results obtained for the average value of σ_φ which is certainly, for holographic phase imaging, the most important parameter. Note that the WFT2F method gives the best performance with an average value at 0.035rad, followed by curvelets at 0.07rad, with in addition, the lowest variance with the curvelets over the whole database. This result confirms that given in the paper of Kaufman [16] about the efficiency of wave atoms based methods. The BM3D method (known as the state of the art) gives quite equivalent results than curvelets, but with a larger variance; this suggests that this method is more sensitive to changes in structures. Surprisingly we can notice that ranking exhibits good performances of median filters 9×9 and 11×11 at 0.09rad. They are followed by SPADEDH near 0.1rad. Above the average value of 0.11rad, ranking exhibits all stationary wavelet methods with close similar variance values, excepted for the regularity 1 which is the Haar wavelet. Around the value of 0.13rad are the two Frost filters. Finally beyond 0.2rad are the three less efficient methods, namely Gauss, Lee filter and NLmeans which also have the largest variances over the database. The surprise is from the NLmeans which was presented as close to the state of the art before the emergence of BM3D. This fact can be explained by considering that the fringe patterns contain areas of continuous curves which affect the search for similar patches in the near vicinity. Thus, the algorithm calculates averaged patches that include major distortions compared to the original image.

Figure 6(b) shows results obtained for the SNR gain. The ranking exhibits strong similarities to that in Fig. 6(a). Note the fairly clear predominance of the WF2TF method that is, with an average gain at 23dB, almost 6dB upon the curvelets which is second best method in the ranking for the SNR gain criterion. The variances associated with median filters are among the lowest. As in Fig. 6(a), stationary wavelets are all in the lower dB range with very close variances excepted for the Haar wavelet. The Lee filter and the linear Gaussian filter exhibit the worst results with less than 9dB of SNR gain.

Figure 6(c) shows the ranking obtained for the Q_{index} criterion. This criterion is related to the quality of the image within the meaning discussed in [15]. Figure 6(c) shows similarities with the previous criteria. Best performance is still once achieved with WFT2F method for which the optimal value is almost reached, just followed by SPADEDH with a Q_{index} value around 0.9. Note the good performances of the median filter methods at about 0.9 excepted for the 7×7 median filter. Curvelets, contourlets and BM3D exhibit good performances and very close variances. As for the other two criteria, performances of all stationary wavelets are similar. The Frost filter has average performances and is ranked just below the stationary wavelets at 0.78. This remark is also true according to the four criteria. It may also be noted that all wavelet methods are not influenced by variations inherent to structural changes in the fringe patterns as they exhibit low variances. Figure 6(d) exhibits ranking obtained for the *SDR* criterion. Even if ranking is not exactly similar to those shown on previous figures, there exist strong similarities particularly with the Q_{index}. First of all, we observe that stationary

wavelet family appears as a group with the same ranking and between the extreme values of the criteria. Frost method follows immediately this group. At the end of the ranking we find the Lee, Gauss and NLmeans methods. At the beginning of the ranking are WFT2F, SPADEDH and median filters (11 × 11 and 9 × 9). The Wiener filter constitutes the only strong exception according to the fact that it exhibits the best results. Finally, Contourlets, Curvelets, BM3D and median 7 × 7 methods appears in the same group inside interval of *SDR* values at [6.5dB; 7dB]. In order to view more details in the performance of the studied algorithms, Fig. 6(e) presents the evolution of the average value of σ_φ according to the input signal to noise ratio, for a selection of eight methods: median 9 × 9, curvelets, BM3D, Wiener, NLmeans (7,15,30), Daubechies 8, WFT2F and SPADETH. One observes curves with decreasing slopes, excepted for wavelet methods which all have an inflection around an input SNR between 6dB and 7dB. The reason is related to the calculation of the threshold for selection of the wavelet coefficients. The threshold is obtained from an estimate of the noise level included in the signal with the Donoho rule, which presupposes sufficiently high noise level. When this assumption is no longer true, the calculated threshold is too high and the threshold causes the loss of the wavelet coefficients associated with the useful signal. Then, it follows that the useful signal is distorted when the SNR increases. In the range [3dB,6dB] which corresponds to reasonably realistic conditions in digital holography, the curvelets method appears to be the best one, if one excepts the WFT2F method. Figure 6(e) also shows that this trend is slightly increased when the input SNR decreases. Beyond 7.5dB, BM3D filter outperforms all the other methods except the WFT2F method. One can also observe some noticeable variations for SPADEDH particularly with lower input SNR. This remains true according to Q_{index} and G_{SNR} criteria. The noticeable superiority of WFT2F method can be understood as, first, because of its complex representation, it is spatially invariant by translation, unlike contourlets and curvelets, second, the waveforms that make up its representation include all possible orientations from the kernel of a two-dimensional fast Fourier transform, unlike stationary wavelets that propose only three orientations.
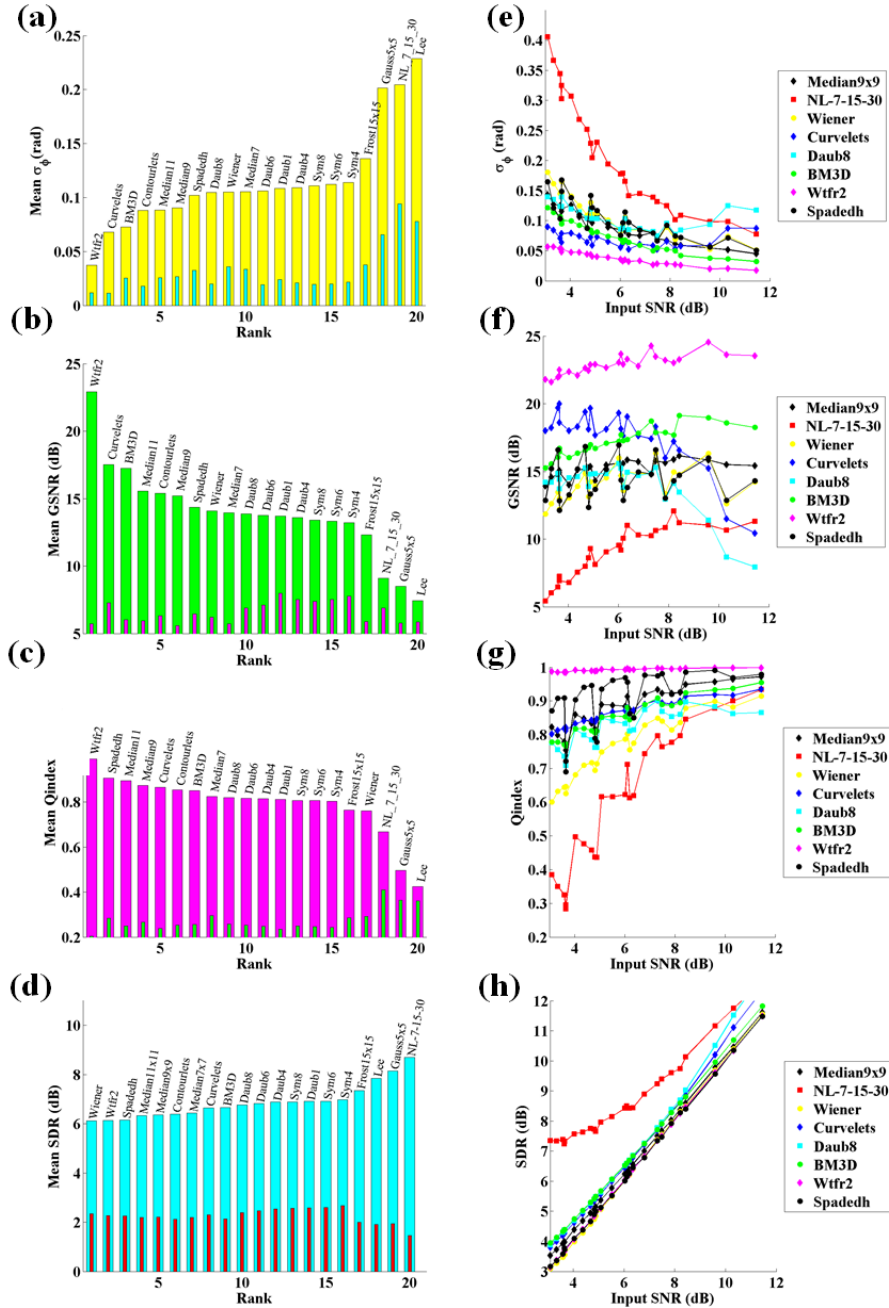
Fig. 6. (a) results obtained for the average value of σ_φ, (b) results obtained for the signal to noise ratio gain, (c) ranking obtained for Q_{index}, (d) ranking obtained for SDR, (e) evolution of the average value of σ_φ according to the input signal to noise ratio, (f) detail of the performance with the SNR gain according to the input SNR, (g) performance of the selected methods regarding to the Q_{index}, (h) performance of the selected methods according to the SDR.

The detail of the performance with the SNR gain according to the input SNR is given in Fig. 6(f) for the selected eight methods. One observes curves with a slow positive slope, excepted for wavelets and curvelets which exhibit an inflection around 8dB for the same reasons as it was observed for Fig. 6(e). On one hand, one observes relative invariant results

for the 9 × 9 median filter which exhibits slow increase, on the other hand this method presents the lowest variance among all methods regarding output SNR gain as can be seen in Fig. 6(b). WFTF2F and BM3D methods show similar behaviors separated with about 6dB. In a similar way, the Wiener filter exhibits slow increase trend but with an increasing variance. For this method, the noise overestimation factor was set at 20 by empirical tests. By making this factor related to the input noise level, it would certainly be possible to improve the performance of this method. Furthermore, this method gives fairly good results from the point of view of the phase error, which is very important in the context of digital holographic metrology. Lastly, NL-means method exhibits a regular increasing trend with amplitude at 7dB over the range of input SNR which is confirmed by its high variance plotted in Fig. 6(b).

Figure 6(g) shows the performance of the selected methods according to the Q_{index}. The curves show a positive slope as a function of the input SNR, with the exception of the stationary wavelets where an inflection point is observed at 8dB. The WFT2F method outperforms all methods with a value near the maximum allowed by the index on the full range of the input SNR. SPADEDH exhibits very good performances with high variations for low input SNR below 8dB. Curvelets, median filter and BM3D present very close results with a smaller variance for curvelets. Then, the Wiener filter presents better results than previous ones with high variations from 0.6 to 0.9. Also, it can be noted that NLmeans has the largest variation of the amplitude across the entire range, which explains the high variance that is observed in Fig. 6(c). Figure 6(h) shows the performances of the selected methods according to SDR. As this criterion is related to the amount of noise that is removed after the de-noising procedure, it is highly correlated to the input SNR. So, one can observe for the selected methods that the related SDR curves follow a tendency which is close to the first diagonal of the x-y axis. The only exception is for NLmeans for which SDR values stand over the input SNR in a decreasing manner from the left to right of the x axis.

Correlations between the four indices are given in Fig. 7. Figure 7(a) shows correlation between the phase error and the cosine Q_{index}. The color code is used to show a group of five points for each of the fringe patterns. There are 20 different methods and 5 different SNR values, therefore 100 points per fringe patterns are represented. A strong anti-correlation is observed between the two criteria. Note also that all the blue circles form an area that overlooks most of the other points. Blue circles correspond to the results of the methods applied on the first fringe pattern, which has high fringe density at its center. This makes it the most difficult fringe pattern to be processed. The corresponding input SNR are the lowest compared to other fringe patterns.
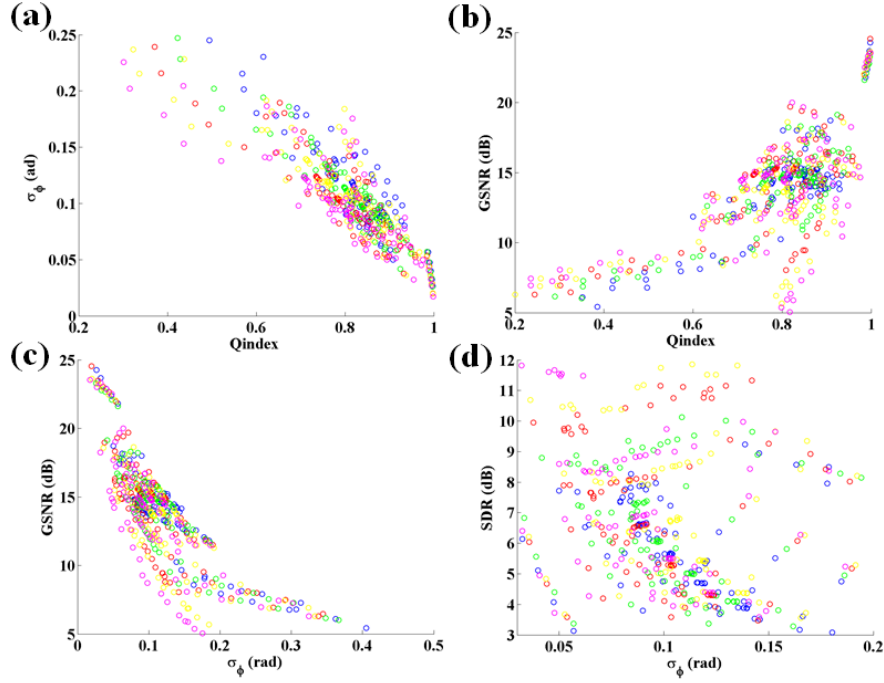
Fig. 7. Correlations between the four indices, (a) correlation between phase error and the cosine Q_{index}., (b) correlation between G_{SNR} and Q_{index}., (c) correlation between G_{SNR} and σ_φ., (d) correlation between SDR and σ_φ.

In Fig. 7(b), there exists a certain correlation between G_{SNR} and Q_{index}. The group of 25 points that can be seen on top right of the Fig. 7(b) corresponds to the WFT2F method. The exponential tendency between the two criteria is due to the logarithmic definition of the SNR gain. The last remark is also true for Fig. 7(c). There exists an increase of the dispersion of the circles due to the increase of the noise level, from the right to the left in Fig. 7(a) and Fig. 7(c), and from top to bottom in Fig. 7(a). Figure 7(c) shows the relationship between G_{SNR} and σ_φ that appears quite similar as an anti-correlation. In a similar way, Fig. 7(d) shows an anti-correlation between SDR and σ_φ but the tendency is clearly less pronounced with a certain amount of points which are located outside the guess curve.
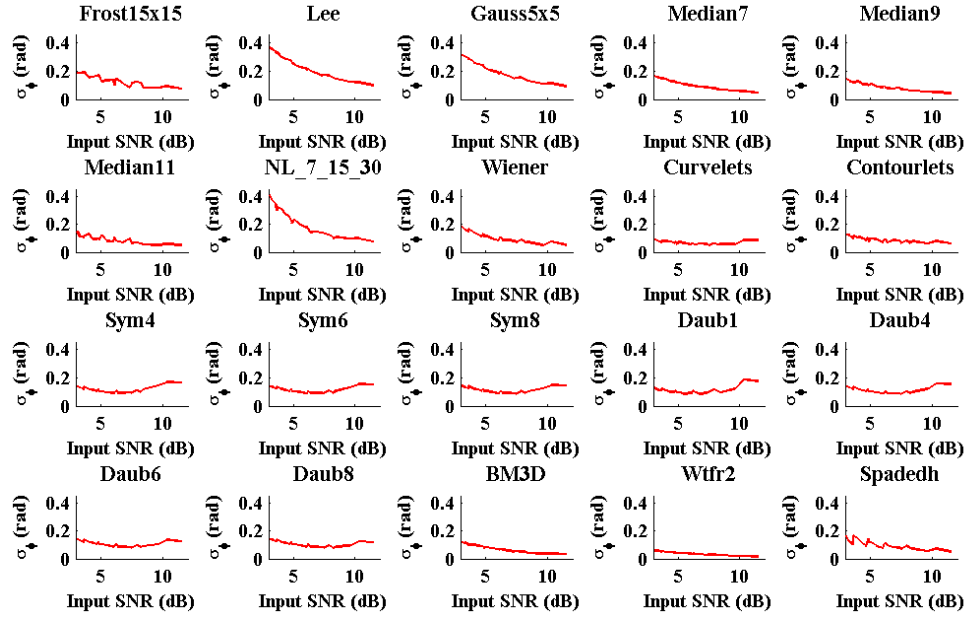
Fig. 8. Trends for the standard deviation of the phase error, σ_φ, versus the input SNR for the 20 selected methods.
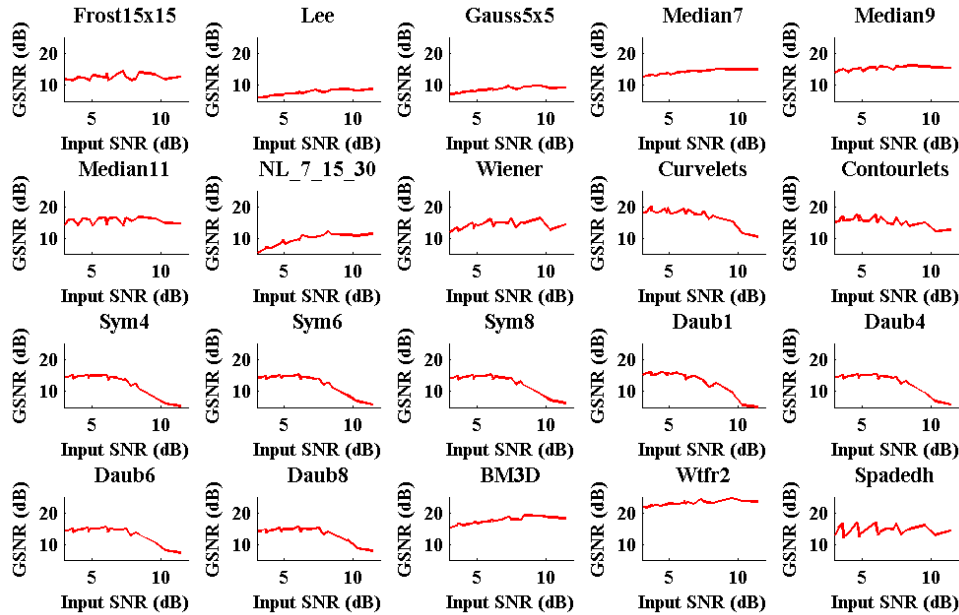

Fig. 9. Trends for G_{SNR} of cosine image versus the input SNR for the 20 selected methods.

Figure 8 to Fig. 11 respectively show the trends for σ_φ, G_{SNR} of cosine image, Q_{index} and SDR versus the input SNR for the 20 selected methods. As can be seen, there already exists the non-monotonic trends for methods based on wavelet with a rise for σ_φ, (Fig. 8), and a decrease for G_{SNR} (Fig. 9) and Q_{index} (Fig. 10) for the higher value of the input SNR. As observed on previous Fig. 6(h), SDR is strongly correlated to the input SNR.

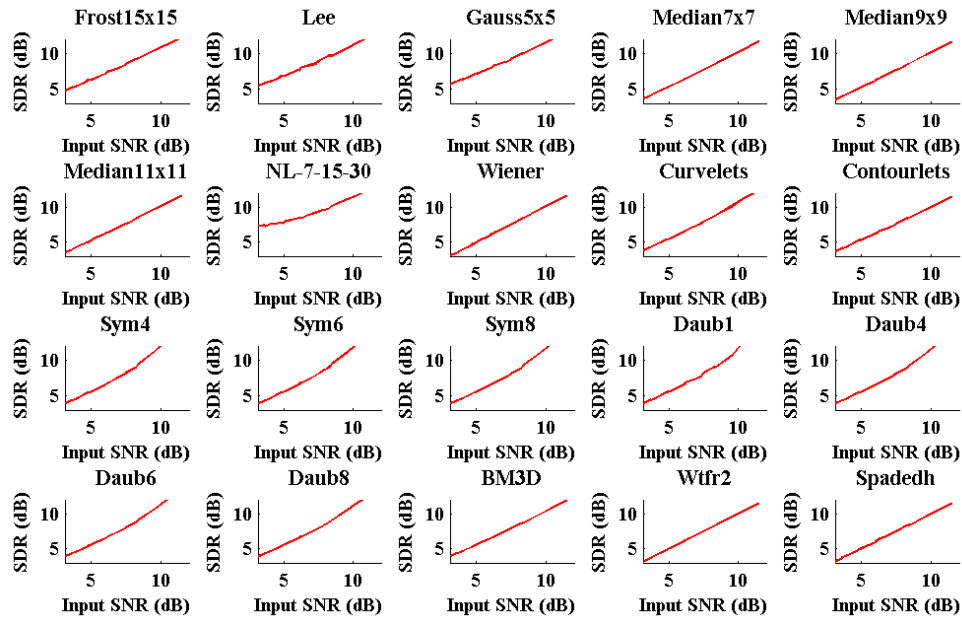Fig. 10. Trends for Q_{index} versus the input SNR for the 20 selected methods.

Fig. 11. Trends for *SDR* versus the input SNR for the 20 selected methods.

7. De-noising of phase fringe patterns

As an illustration of de-noising of phase maps, Fig. 12 shows results obtained with processing the first fringe pattern in 1st column in Fig. 5. The input SNR is at 3.01dB for the cosine image. Figure 12(a), Fig. 12(c), Fig. 12(e), Fig. 12(g), Fig. 12(i) and Fig. 12(k) exhibit the filtered phase obtained with respectively BM3D, curvelets, NLmeans (7,15,30), 9 × 9 median, WFT2F and Daubechies 8. Figure 12(b), Fig. 12(d), Fig. 12(f), Fig. 12(h), Fig. 12(j) and Fig.

12(l) shows the corresponding residual phase noise. One clearly observes that there remains a large amount of noise with NLmeans method (Fig. 12(f)). Curvelets and WFT2F (resp. Figures 12(c) and 12(i)) exhibit the best de-noised phase images.
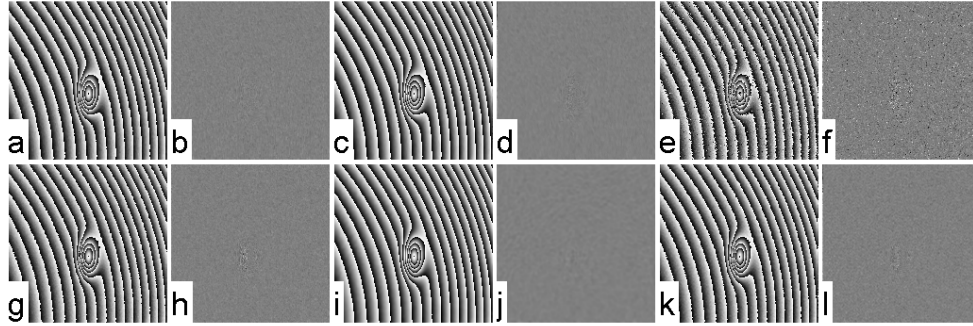

Fig. 12. De-noising of the 1st fringe pattern of Fig. 5 (1st column), (a) processing with BM3D, (b) corresponding residual noise, (c) processing with curvelets, (d) corresponding residual noise, (e) processing with NLmeans (7,15,30), (f) corresponding residual noise, (g) 9 × 9 median, (h) corresponding residual noise, (i) WFT2F, (j) corresponding residual noise, (k) Daubechie 8, (l) corresponding residual noise.

Figure 13 shows a phase map obtained with an off-axis digital holography set-up ref [44] which was processed with WFT2F. Figure 13(a) exhibits the noisy experimental phase and Fig. 13(b) shows the result after processing by WFT2F with the same conditions as for the benchmark. Figure 13(c) shows the residual phase noise.
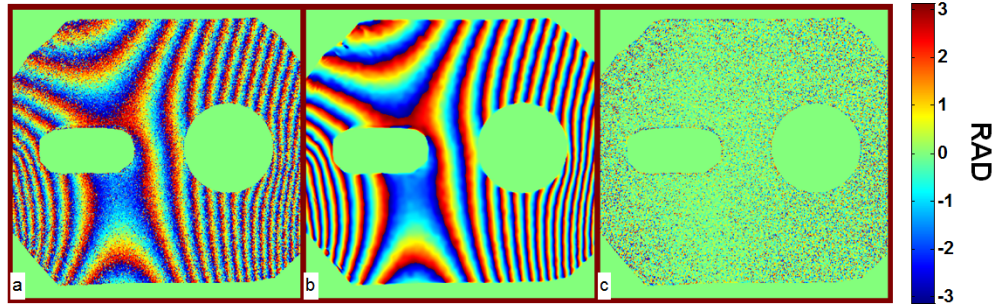

Fig. 13. Experimental phase processed with WFT2F, (a) noisy phase map, (b) filtered phase map using WFT2F, (c) residual noise estimated from the processing.

8. Conclusion and perspectives

This paper presents a quantitative comparison of algorithms for speckle decorrelation phase noise removing in digital holography. For the evaluations, a noisy fringe pattern simulator generating realistic phase images has been proposed. Statistics of decorrelation noise are in conformity with those found in real phase data. The main advantage of the phase simulator is that it provides phase image including decorrelation phase noise and that filtering algorithms can be compared by quantitatively evaluating the noise reduction. A database, including 25 fringe patterns divided into 5 patterns and 5 different signal-to-noise ratios, was generated to evaluate the selected algorithms. We have retained four evaluation criteria: the overall standard deviation error on the phase, the gain in the signal-to-noise ratio, the quality index which is an objective test rendering the sensitivity to distortions in fine image structures, and the signal to distortion ratio which applies without the need of reference noise-free image. The standard deviation phase error has the highest relevance for the point of view of digital holographic metrology. A total of 34 algorithms divided into different families were

evaluated. The selected algorithms are: the linear Gaussian filter, the median filter, the Lee filter, the Frost filter, the Wiener filter, the stationary wavelets including Daubechies and symlets wavelets, curvelets and contourlets, the NLmeans filter the BM3D filter, the WFT2F filter and the SPADEDH algorithm.

In terms of phase error, it appears that the WFT2F method offers the best results with an average error at 0.035rad. With an average error of 0.07rad, the second position in the ranking is occupied by the curvelet decomposition, especially when the noise level is high. The BM3D filter, which currently represents the state of the art in the field of image de-noising, yields very similar results, and even slightly better for an input SNR 6dB higher, but with a higher sensitivity to the fringe pattern structures.

A similar ranking is observed for the three other criteria, excepted for SPADEDH, 9×9 and 11×11 median filters for which it was demonstrated their very good performance in terms of Q_{index} and SDR. Note also that these three algorithms achieve better results for the four criteria than stationary wavelet methods. Furthermore, a fairly good correlation between the SNR gain and the quality index has been observed, excepted for the Wiener filter. There exists an anti-correlation between the phase error and the quality index which indicates that the phase errors are mainly structural distortions in the fringe pattern.

Future work include assessment of the noise level in the fringe pattern in order to adequately adjust the threshold which, in particular, determines the performance of the algorithms based on wavelets, curvelets and contourlets. A second track may consist in evaluating a possible phase error generated by the noise reduction methods that could be depending on the input noise, the ultimate goal being to get robust estimators in terms of phase metrology based on digital holography.

Acknowledgments